IEEE Access
Multidisciplinary ⋮ Rapid Review ⋮ Open Access Journal

Received 5 March 2024, accepted 9 April 2024, date of publication 15 April 2024, date of current version 26 April 2024.

Digital Object Identifier 10.1109/ACCESS.2024.3388494

RESEARCH ARTICLE

A Drone-Driven X-Ray Image-Based Diagnosis of Wind Turbine Blades for Reliable Operation of Wind Turbine

HYUNYONG LEE, YU MIN HWANG, (Member, IEEE), JUNGI LEE, NAC-WOO KIM, AND SEOK-KAP KO
Electronics and Telecommunications Research Institute, Buk-gu, Gwangju 34129, South Korea

Corresponding author: Yu Min Hwang (yumin@etri.re.kr)

This work was supported by Korea Institute of Energy Technology Evaluation and Planning (KETEP) funded by Korean Government (MOTIE) through the Development of an X-Ray-Based Non-Destructive Inspection Platform for Maintaining the Blade Lightning System for Wind Power Generation under Grant 20223030020070.

ABSTRACT In this paper, we propose methods for the diagnosis of down conductor cables installed inside blades for the reliable operation of wind turbines. Utilizing the two synchronized drones equipped with X-ray devices to take X-ray images inside the blades, we propose deep learning methods for diagnosis based on X-ray images. The first method is the unsupervised deblurring method for blurry X-ray images that are generated by the drones. The key idea of the proposed method is to apply an image sharpening process to the latent space of the trained model using only blurry X-ray images. Through experiments using the X-ray images of blades, we show that the proposed method makes the outline of the down conductor cable clearer. As the second method, we propose an object detection-based method to provide fast and accurate object detection as the diagnosis. Given an X-ray image, we also propose a method to determine drone flight direction to enable drones to follow the down conductor cable. Through experiments, we show that our method has good performance in object detection (i.e., mAP of 98.21%) and classification (i.e., AUC of 0.9), and drone flight direction determination (i.e., AUC of 0.99).

INDEX TERMS Wind turbine, lightning protection system, blade, down conductor cable, X-ray image, drone, diagnosis, deep learning.

I. INTRODUCTION

Global renewable energy adoption is increasing to achieve greenhouse gas reduction and carbon neutrality [1], [2]. The proportion of renewable energy in the world's electricity mix is gradually increasing. In the case of two prominent renewable energy sources, solar power generation, and wind power generation, the share of electricity generation capacity as a percentage of total power production was 2.19% and 4.86% in 2018, 2.66% and 5.38% in 2019, 3.24% and 6.04% in 2020, 3.74% and 6.64% in 2021, and 4.52% and 7.5% in 2022, respectively [3]. In the case of wind power generation, it is projected to increase by an average of approximately 15% annually (from 78GW to 157GW) in terms of generation capacity from 2022 to 2027 [4].

Wind turbines have grown in both hub height (i.e., the distance from the ground to the turbine rotor) and blade lengths to generate more energy [5]. Building a taller turbine tower is important in capturing more energy since winds generally increase as altitudes increase. The average hub height has increased from 80 meters in 2010 to 100 meters in 2022. The average hub height for offshore wind turbines in the United States is projected to grow to about 150 meters in 2035 [6]. Longer blades enable wind turbines to sweep more area, capture more wind, and thus produce more electricity. The average rotor diameter (i.e., the width of the circle swept by the rotating blades) has increased from less than 100 meters to 130 meters in 2022 [6].

The associate editor coordinating the review of this manuscript and approving it for publication was Moussa Boukhnifer.

Wind turbines are typically installed in locations where wind is abundant, and there are minimal or no obstructions in the surrounding areas. For this reason, wind turbines are directly exposed to external environmental factors, and over time, their initial performance can deteriorate, or they may suffer damage. When issues arise with wind turbines, analyzing the causes and carrying out replacements of the affected components can result in a significant decrease in power generation, leading to a drop in revenue for the power company. With the increasing scale of wind turbines, the risk of lightning strikes also rises. Therefore, the continuous monitoring and maintenance of lightning protection systems (LPSs) [7] installed on wind turbines are essential for stable operation. Particularly, early detection of structural defects in the external and internal components of the blades (e.g., the receptor and the down conductor cable), which are the primary points of lightning strikes, is of utmost importance. In this study, we focus on the diagnosis of the down conductor cables located inside the blades of wind turbines as a part of LPS. In particular, we adopt a non-destructive diagnosis approach.

Various techniques for non-destructive diagnosis of the blades have been proposed [8]. Existing methods for non-destructive diagnosis can be categorized into three perspectives: the data used, how a drone is utilized, and what kind of diagnosis algorithm is used. Existing methods try to utilize various types of data including RGB images [9], [10], [11], [12], [13], [14], [15], [16], [17], [18], ultrasonic testing [19], [20], [21], [22], acoustic emission [23], [24], [25], [26], [27], [28], [29], [30], tomography [31], [32], and thermography [33]. However, they mostly focus on detecting damage on the surface of the blades. Many works utilize the drone for acquiring diagnosis data [11], [12], [13], [34], [35]. However, most existing drone-based methods support visual inspection whose application is limited to the surface of blades. Existing methods try to combine feature extraction engineering with robust methods based on data-driven analysis, machine learning, and artificial neural networks [9], [10], [11], [12], [13], [14], [15], [16], [17], [18]. However, most existing methods did not consider automated data acquisition and unmanned real-time monitoring, which may limit their application in wind farms.

To overcome the limitations of existing methods and ensure the stable operation of wind turbines, an effective method for diagnosing the interior of the blades is essential. Our research aims to develop a non-destructive blade internal diagnosis technology that can reduce inspection time and costs while achieving good diagnosis accuracy. Our research primarily involves the development of three key technologies:

A. X-RAY DEVICES

We developed lightweight and human-safe low-dose digital X-ray devices including an X-ray generator and an X-ray detector, designed to be mounted on two drones.

B. DRONES

We developed a drone in consideration of application to wind turbine blades and installation of X-ray devices. We also developed drone swarm control technology to facilitate X-ray imaging by synchronizing drones.

C. DEEP LEARNING DIAGNOSIS

We developed deep learning methods for blade internal diagnosis based on X-ray images: unsupervised deblurring of X-ray images and object detection-based diagnosis with the deblurred X-ray images. Given X-ray images by synchronized drones, the first goal is to make blurry X-ray images clear. One challenging issue is that blurry and clear X-ray image pairs (that are typically used for training a deep learning deblurring model) are not available. To solve this issue, we train an autoencoder-style model with only blurry X-ray images and then apply an image sharpening process in the latent space of a trained model. We intend to enhance the deblurring performance through image sharpening process in the latent space where the blur effect is somewhat reduced. Through experiments using the drone-driven X-ray images of a wind turbine blade acquired from our testbed, we show that our method makes the outline of the object of interest in the image (i.e., down conductor cable) clearer.

The next goal is to detect the down conductor cable and determine its state (i.e., normal or abnormal) using the deblurred X-ray images. We adopt an object detection-based approach using YOLOX-Tiny [36] which shows a good balance between high detection precision and high detection speed. One requirement is to determine drone flight direction using X-ray images for realizing autonomous flight during a diagnosis of blades. To satisfy the requirement, we propose Xray-YOLOX-Tiny by modifying YOLOX-Tiny. Through experiments using the X-ray images of a wind turbine blade, we show that Xray-YOLOX-Tiny supports accurate drone flight direction determination (i.e., AUC of 0.99) while sustaining the performance of object detection (i.e., mAP of 98.21%) and classification (i.e., AUC of 0.9) with a slight increase in the number of parameters and execution time over YOLOX-Tiny.

The main contributions of our research are as follows: 1) we have developed drones capable of mounting X-ray devices and synchronized drone swarm control, 2) miniaturized X-ray devices to be mounted on drones, and 3) object detection-based diagnosis and drone flight control technologies for wind turbine blade diagnosis and verified their performances on the testbed. Above all, our approach is the world's first wind turbine blade diagnosis attempt using drone-driven X-ray images.

The rest of this paper is organized as follows. Section II describes the background of our work including LPS and related work. Section III introduces an overall overview of our research (i.e., a drone-driven X-ray image-based diagnosis) together with the developed prototypes and the testbed. Section IV proposes and verifies the unsupervised deblurring

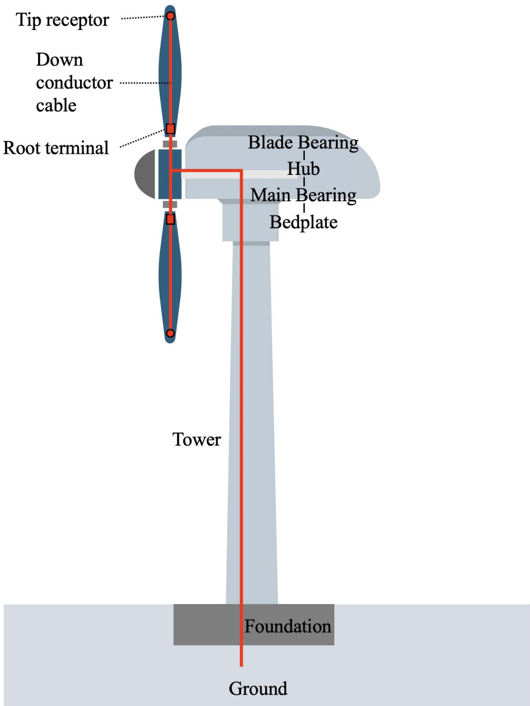

FIGURE 1. **A high-level overview of the lightning protection system of a wind turbine.**

technique to make blurry X-ray images clearer. Section V discusses object detection-based diagnosis and drone flight direction control. Finally, Section VI concludes this paper.

II. BACKGROUND

A. LIGHTNING PROTECTION SYSTEM

Wind turbines are typically installed high in open and exposed environments and are easy to be directly exposed to lightning. Lightning can disrupt the normal operations of wind turbines or physically destroy blades. To keep wind turbines safe from lightning, wind turbines are equipped with LPS. LPS serves as a grounding path for lightning once it strikes the wind turbine to protect a wind turbine. Fig. 1 shows a high-level overview of LPS from the perspective of the path for the electric current throughout the wind turbine. If lightning strikes at any receptor of a wind turbine blade, the lightning current is conducted to the ground via down conductors, root terminal, blade bearing (i.e., pitch bearing), hub, main bearing, bedplate, tower, and foundation.

For LPS to function properly, each component that constitutes LPS must operate normally and be well connected. If not, lighting strikes can significantly damage a wind turbine because the lightning is not correctly routed to the ground. In an attempt to realize the reliable operation of wind turbines, in this paper, we focus on the down conductor cable, which is the second part of LPS. Once lightning strikes a tip receptor located on the outer surface of the wind turbine blade, the next part of the LPS path is the down conductor cable which is embedded in the blade. Down conductor cables have a chance of being damaged. For example, down conductor cables can be lacerated due to aged deterioration. The enormous energy of lightning current also can enable down conductor cable to be separated [37], [38], [39]. The damaged down conductor cable is likely to cause a problem (e.g., blades can be damaged), particularly if the lightning strikes again.

B. EXISTING SOLUTIONS FOR NON-DESTRUCTIVE DIAGNOSIS

Non-destructive diagnosis is commonly used for wind turbine blades [8]. We categorize the existing solutions for non-destructive diagnosis into three perspectives: the data used, how a drone is utilized, and what kind of diagnosis algorithm is used.

1) DATA

Advanced techniques for the non-destructive diagnosis include visual inspection (i.e., RGB images) [9], [10], [11], [12], [13], [14], [15], [16], [17], [18], ultrasonic inspection [19], [20], [21], [22], acoustic emission [23], [24], [25], [26], [27], [28], [29], [30], tomography [31], [32], and thermography [33]. *(Visual inspection)* Visual inspection is a useful technique for quickly observing surface-breaking discontinuities on wind turbine blades. In [9], the authors utilized RGB images obtained from drones to identify blade cracks by capturing Haar-like features for surface cracks on wind turbine blades. In [10], the authors proposed a modified speeded-up robust features (SURF)-enhanced digital image correlation algorithm combining an angle compensation strategy to detect cracks using the surface strain field of wind turbine blades. In [11], the authors proposed a deep learning-based automated damage inspection system to classify four damage classes based on a digital camera-equipped multi-copter UAV. In [12], the authors focused on a digital camera-equipped UAV-based blade inspection method with pre-trained CNNs, which were integrated with their image dataset via transfer learning. In [13], a digital camera-equipped UAV-based multiple-class fault classification model for structural health monitoring of wind turbine blade inspection has been developed. In [14], [15], and [16], deep learning-based fault detection of wind turbine blade inspection with RGB images has been done. In [17] and [18], authors conducted research on acquiring 3D digital images and detecting deformation. *(Ultrasonic inspection)* In [19] and [20], the authors utilized ultrasonic signals and ultrasonic guided waves to examine the multi-level ice thickness distribution on the surface of wind turbine blades. In [21], the authors proposed an ultrasonic phased array technique. In [22], ultrasonic-based monitoring techniques for the wind turbine gearboxes were proposed. *(Acoustic emission)* The acoustic emission-based detection technology captures the blade aerodynamic noise signal and can detect the potential for blade damage and its location [23], [24], [25], [26], [27], [28], [29], [30]. In [30], the authors conducted a comprehensive review of non-destructive, real-time health monitoring of wind power blades based on acoustic emission signals. *(Tomography)* Electrical impedance tomography was used in [31] to propose self-sensing for piezoresistive nanocomposites. In [32], wind turbine blades were analyzed based on X-ray tomography. *(Thermography)* In [33], the variational asymptotic multiscale method was developed as a dimensional reduction model to analyze the thermoelastic behavior of wind turbine blades. ***(Ours)*** Most existing methods have focused on detecting damage on the surface of the blades. On the contrary, we propose a drone-driven X-ray image-based method to not only detect but also continuously track and scan the object of interest installed inside the blades. This method allows for the identification of the location, type, size, and shape of various damages that can occur inside the blade, not on the surface.

2) DRONE

Expert-based classic visual inspection can be replaced with drone-based methods. In [11], [12], and [13], the authors commonly proposed an inspection method based on a digital RGB camera-equipped multi-copter UAV. Utilizing a multi-copter, blade images are acquired, and a damage feature is learned using a data-driven method, followed by a diagnosing method to determine the location and type of damage. In [34], authors proposed a UAV-based digital image correlation-based blade structure monitoring using a stereo camera system. In [35], for automated maintenance of wind turbine blades, authors proposed multi-robot-approach with climbing robot and multi-copters with vision and LiDAR sensors. ***(Ours)*** Most existing drone-based methods support visual inspection whose application is limited to the surface of blades. On the contrary, we developed miniaturized X-ray equipment that can be mounted on a drone. We also developed synchronized drone swarm control technology for X-ray imaging. Unlike conventional drone-based methods based on RGB images, our method can diagnose internal damage of blades.

3) ALGORITHM

The non-destructive diagnosis typically combines feature extraction engineering with robust methods based on data-driven analysis, machine learning, and artificial neural networks. In [9], the authors applied Haar-like features to identify real-time surface cracks on wind turbine blades using RGB images. In [14], Alexnet, and in [15] and [16], YOLO-based fault detection of wind turbine blade inspection has been done. In [10], the authors examined the operating structural characteristics of the rotating blades with digital image correlation. The proposed angle compensation (AC)-SURF algorithm detects and recognizes the relative strain distribution caused by flaws and any damage to the wind blades. In [17] and [18], digital image correlation-based structural monitoring of wind turbine blades has been done. In [11], the authors proposed a deep learning-based feature extraction methodology to identify four damage classes based on RGB images. In [12], the authors focused on transfer learning-based feature engineering to utilize their image dataset. In [13], a multiple-class fault classification model for wind turbine blade inspection has been developed. ***(Ours)*** Most existing methods did not consider automated data acquisition and unmanned real-time monitoring, which may limit their application in wind farms. On the contrary, we utilized the well-known lightweight data-driven object detection model, YOLOX-Tiny, to improve response speed and detection accuracy for real-time diagnosis, and added the functionality of detecting the direction of objects based on X-ray images for autonomous drone flights along with the down conductor cable inside the blades. Additionally, we developed a deblurring technique to improve blurry X-ray images captured by the drone.

Our method is similar to an ongoing project, SpectX [40], [41]. Using X-ray technology and a drone platform, SpectX aims to provide non-invasive and high-resolution scans of blades. In particular, SpectX focuses on hidden damage, including delamination, cracks, and holes. On the contrary, we utilize X-ray equipment and drones to examine the down conductor cable inside the blades. We consider some issues that are ignored in existing solutions including SpectX. We propose a method for deblurring blurry X-ray images taken by drones. We also propose a method for determining drone flight directions to enable drones to follow the down conductor cable inside the blade, thus realizing autonomous flight without prior information about down conductor cable layout.

III. A DRONE-DRIVEN X-RAY IMAGE-BASED DIAGNOSIS

A. FRAMEWORK

Fig. 2 shows an overall framework of a drone-driven X-ray image-based diagnosis and the focus of this paper. The issues discussed in this paper are highlighted with a red-dotted box in Fig. 2. The framework includes two drones with X-ray devices, a ground control station (GCS), an image server, and a diagnosis and control server.

The position of the two drones is controlled and synchronized using a real-time kinematic-global positioning system (RTK-GPS) [42]. One of the two drones is equipped with an X-ray generator (i.e., Drone #1 in Fig. 2) that generates X-rays. The other drone is equipped with an X-ray detector (i.e., Drone #2 in Fig. 2) that generates digital X-ray images. In this way, the two drones generate X-ray images of the inside of the wind turbine blades.

The GCS communicates with the drones to control them. The two drones and the GCS are equipped with the same communication module (e.g., WiFi, LTE, and so on). The communication is done through the communication channel implemented by the communication module. Once X-ray imaging is done, the GCS guides the drones to other places for further X-ray imaging if required.

The image server acquires the X-ray images from the drone equipped with an X-ray detector. For this data transfer, the image server and the drone equipped with an X-ray detector are with the same communication module. The image server stores X-ray images in the database. Also, the image

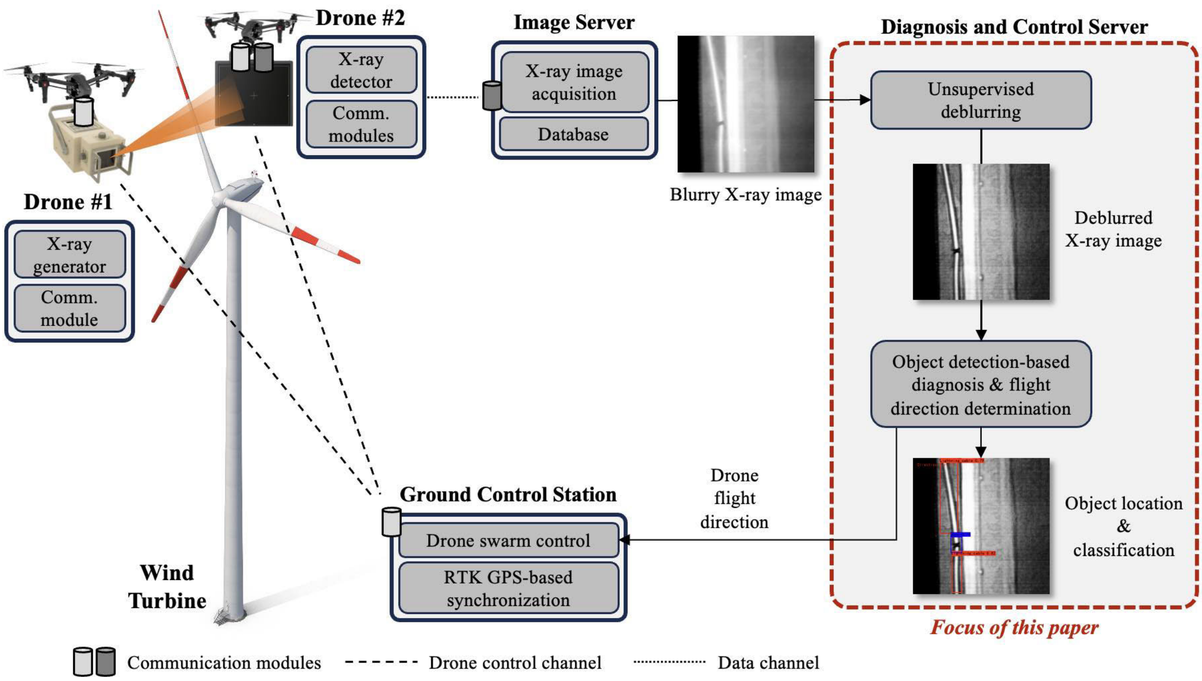

FIGURE 2. **Overall framework of our research and the focus of this paper.**

server sends a newly acquired X-ray image to the diagnosis server.

The diagnosis server applies several deep learning techniques that will be discussed in this paper. The first technique is deblurring. The X-ray devices used in the framework are low-dose X-ray devices. The low-dose X-ray devices take around 100 milliseconds to generate an X-ray image. An inevitable and subtle movement of drones during X-ray imaging and low-dose X-rays are likely to cause a blur effect in X-ray images. To this end, we need to conduct deblurring of blurry X-ray images as a pre-processing. The next step is to conduct a diagnosis. For this, we first detect objects of interest (i.e., down conductor cable) and then classify the detected object as normal case or abnormal case. Finally, we need to guide the drones for further X-ray imaging if required. Please note that we cannot calculate the flight direction of the drones in advance because we do not know the position of the down conductor cable. If we can have the information about the layout of the down conductor cable in advance (e.g., blueprint), we may be able to calculate the flight path in advance and this case is out of the focus of this paper. We determine the flight direction of the drones for the next movement using the X-ray image. Once the flight direction is determined, the determined flight direction is sent to the GCS. Then, the GCS controls the drones according to the given flight direction.

B. PROTOTYPES

1) X-RAY DEVICE

Our goal is to build a low-weight X-ray device to be easily equipped with the drone. For this, we developed a lightweight

FIGURE 3. **An X-ray generator prototype.**

X-ray generator weighing 6.0 kilograms through lightweight design (Fig. 3). We develop a low-dose X-ray generator that can operate at a power range of 450W to 1.2kW to minimize radiation exposure to the human body. During a single imaging session, we confirmed a radiation dose of 0.4 microsieverts, which is at the level of natural background radiation. Due to the low-dose nature of the X-ray generator, X-ray imaging takes approximately 100 milliseconds to complete. The resolution of an X-ray image is $3{,}012 \times 3{,}012$. The X-ray generator operates using a separate battery of 5,000mAh.

2) DRONE

We developed two drones for our purpose: one with an X-ray generator and the other with an X-ray detector (Fig. 4). The drone was developed considering the wind power generation environment to which the drone is to be applied. Wind turbines are generators that produce electricity, and as a result of generation, they can create strong magnetic fields. Therefore, due to the strong magnetic fields that can be created by operating wind turbines rather than an inspection target, issues such as abnormal operation or even crashes of

(a) The drone with an X-ray generator.

(b) The drone with X-ray detector.

FIGURE 4. **The drone prototypes with an X-ray devices.**

FIGURE 5. **A testbed installed in an open outdoor space.**

drones can occur. To address these potential issues, the digital compass function was replaced with the dual antenna feature of RTK-GPS, eliminating the need for a digital compass, which can be affected by magnetic fields. The drones are equipped with LiDAR sensors to keep a distance from the wind turbine blade and avoid collisions. Currently, the drones are set to maintain a distance of 3 meters from the blade. The maximum distance between the two drones for X-ray imaging is 12 meters. To prevent shaking or instability in the imaging results during drone flight and capture, a three-axis gimbal was mounted on the drone with an X-ray generator.

The two drones need to be synchronized for X-ray imaging. In the case of an X-ray generator, there is a specific range of examination, and this varies depending on the distance from the object being examined, which in turn affects the range and results of the imaging. Therefore, the X-ray detector must exist within the examination range of the X-ray generator, which allows for obtaining imaging results at the desired locations of blades. To realize the synchronized control of two drones, we utilize two technologies: RTK-GPS and micro air vehicle link (MAVLink) [43]. RTK-GPS utilizes a GPS base station installed at a location where the latitude/altitude/longitude is known in advance. The GPS base station can calculate the error of the received GPS signal because it knows its current exact location. The GPS base station transmits the calculated error of the received GPS signal to a GPS rover (i.e., a GPS device mounted on a drone) to correct the GPS signal. RTK-GPS provides 1-2-centimeter accuracy while traditional GPS typically offers 2-5-meter accuracy. MAVLink is a light messaging protocol designed to support communication between small unmanned vehicles such as drones. For two drones to share their positions determined by RTK-GPS, communication based on MAVLink is utilized. MAVLink allows quick exchange of flight information including location, and commands between drones, allowing them to determine each other's locations in real-time and perform synchronized flights.

The weight of the drone is 20 kilograms. The maximum flight speed is 7 meters per second. The maximum takeoff weight is 24.9 kilograms. The propulsion system is an electric motor. The drone's dimensions are 1240×1240 x 800, with width x length x height in millimeters.

C. TESTBED AND DATASET

1) TESTBED

Fig. 5 shows our testbed to examine the feasibility of the drones, the X-ray devices, and our diagnosis techniques. To build an environment similar to the environment in which actual wind turbine blades are installed and operated, a testbed was installed in an open outdoor space. Fig. 6 shows a scene of experimenting with drone and X-ray device prototypes on the testbed. The drone on the left side in Fig. 6 is equipped with an X-ray generator, and the drone on the right side in Fig. 6 is equipped with an X-ray detector. For a blade sample in the testbed, we cut off the real blade once used for wind power generation. We made a sample measuring $10 \times 1.1 \times 0.3$ meters by cutting a blade 10 meters away from the blade tip of a 3 MW-class wind turbine (i.e., a blade length of 65 meters).

2) DATASET

To acquire the X-ray images of wind turbine blades for training deep learning models, we conducted repetitive experiments with the drone and X-ray device prototypes as shown in Fig. 6. For data acquisition, we manually controlled the drones.

FIGURE 6. An experiment with the drone and X-ray device prototypes.

We needed to label the acquired X-ray images for object detection-based diagnosis and drone flight direction determination, which are supervised learning. The objective of object detection-based diagnosis is to classify the detected down conductor cable into normal or abnormal cases. In this paper, we consider three cases: regular down conductor cable (i.e., Lighting cable as a class throughout this paper), disconnected down conductor cable (i.e., Open as a class throughout this paper), and melted down conductor cable (i.e., Melt as a class throughout this paper). When lighting strikes a receptor of a wind turbine blade, the lighting current is conducted to the earth via down conductor cables. Because the energy of lighting current is enormous, down conductor cables can be disconnected [44], [45], [46], [47]. We also consider another possible case that can happen by the lightning current. By the enormous energy of lighting current, the down conductor cables can be changed in shape (e.g., melt, bent, and so on). In this paper, we assume that deformation of the down conductor cable shape can cause potential problems in handling the lighting current, and thus we want to detect such shape deformation. For the two abnormal cases above, we artificially manipulated those down conductor cables in the testbed. Fig. 7 shows samples of three cases we are interested in this paper. Please note that the red dotted boxes in Fig. 7 are not included in the images themselves, but are used for better presentation. After acquiring X-ray images from the testbed, we manually labeled the X-ray images by inspecting each image. In this case, the label includes the class (i.e., Lightning cable, Open, or Melt), and the coordinates of the bounding box (i.e., coordinates of the area including the down conductor cable). The number of X-ray images for Lightning cable, Open, or Melt classes is 1,253, 182, and 533, respectively. The total number of acquired X-ray images is 1,968.

Another labeling issue arises about drone flight direction determination. Please note that all the acquired X-ray image is directed in the north direction as shown in Fig. 7 and that the down conductor cables can be installed in various directions inside a blade. In addition, the direction of the down conductor cable varies depending on the direction of the blade to be inspected. To handle this issue, we apply a rotation-based data augmentation technique to simulate down conductor cables connected in different directions. For this, in addition to the north direction, we apply seven additional directions (i.e., northwest, west, southwest, south, southeast, east, and northeast). In this case, the label is the direction used for the augmentation. At this time, the coordinates of the down conductor cable inside the X-ray image are also converted accordingly and can be used for object and direction classification learning. Fig. 8 shows an example of rotation-based augmentation.

IV. UNSUPERVISED DEBLURRING OF X-RAY IMAGES

A. OBJECTIVE AND CHALLENGING ISSUES

The X-ray images taken by drones are likely to be blurry. The low-dose X-ray generator worsens the blurriness. The X-ray images need to be as clear as possible because they are used as basic data for deep learning models for diagnosis and human readings. In particular, the object of interest must be clearly expressed. For this, we conduct a deblurring of X-ray images. In implementing the deblurring of X-ray images, we need to consider the following challenging issue. In the target environment of our research, clear X-ray images corresponding to blurry X-ray images are not available. Please note that it is impossible to generate clear X-ray images of the parts taken by the drones with fixed X-ray equipment. Therefore, without the clear X-ray images that are required by most existing deblurring deep learning models, we need to conduct the deblurring of X-ray images. The following subsections describe our unsupervised deblurring model.

B. UNSHARP MASKING IN ORIGINAL SPACE

Before introducing our approach, we briefly describe an existing algorithm related to our approach. Given an original X-ray image, there are several sharpening algorithms to be applied. One of the popular sharpening algorithms is unsharp masking [48]. Unsharp masking is a kind of linear filter that amplifies the high-frequency content of an image. Fig. 10 shows the overall processes of unsharp masking. The first step of unsharp masking is to generate a blurred version of an original image by applying a filter such as a Gaussian filter. Then, we subtract the blurred image from the original image to generate a mask that contains the edges created by the filter. Finally, a sharpened image is generated by adding the mask to the original image. In generating a blurred image, various filters can be used. The available filters include the Gaussian filter, Median Filter, Maximum Filter, and Minimum Filter. Those filters are different in replacing pixel values. For example, the maximum filter replaces each pixel value with the maximum value (i.e., the brightest one) while the minimum filter replaces each pixel value with the minimum

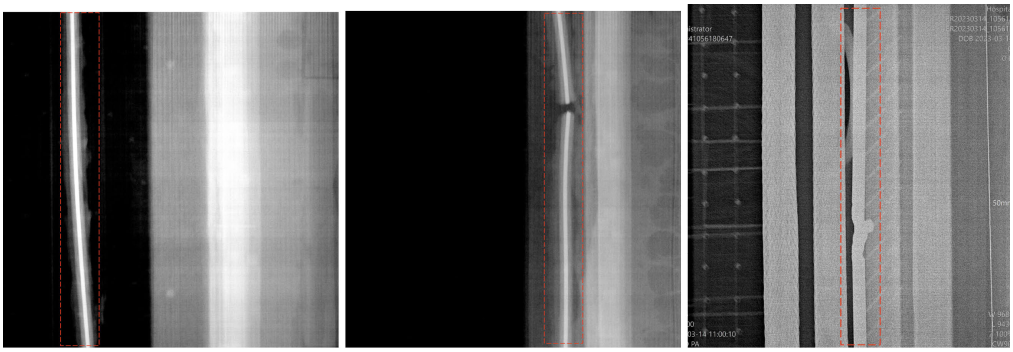

(a) A regular down conductor cable. (b) A disconnected down conductor cable. (c) A melted down conductor cable.

FIGURE 7. Samples of three cases of down conductor cable. The down conductor cable is marked with a red dotted box.

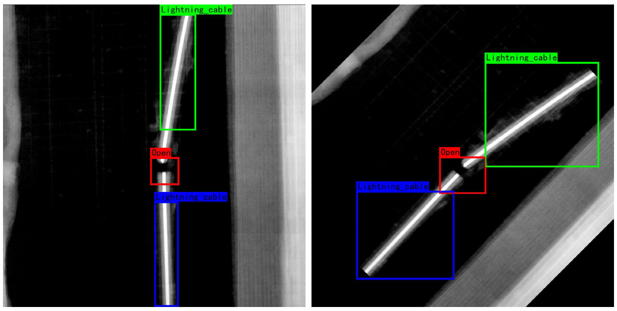

(a) An original X-ray image. (b) An augmented X-ray image.

FIGURE 8. A sample of rotation-based augmentation. Color boxes indicate the coordinates as labels.

value (i.e., the darkest one). Through the experiments with the X-ray images of our testbed, we empirically found that the Maximum filter is a good match for unsharp masking for our purpose.

Applying unsharp masking to the original X-ray images (i.e., in the original space) is simple and fast. However, through the experiments with the acquired X-ray images, we found that using unsharp masking in the original space sometimes fails to make blurry X-ray images clearer. To this end, we propose unsharp masking in latent space with unsupervised learning to improve the sharpening process further.

C. UNSHARP MASKING IN LATENT SPACE WITH UNSUPERVISED LEARNING

1) MODEL ARCHITECTURE

Fig. 9 shows our proposed unsupervised deep learning model for the deblurring of X-ray images and procedures for training the deblurring model. The proposed deblurring model is a convolutional autoencoder. The deblurring model includes two parts: one part for extracting features from an input X-ray image and the other part for reconstructing an X-ray image from the extracted features. The feature extraction part (i.e., encoder) consists of two 2D convolutional layers. The first 2D convolutional layer applies 3×3 kernels and a stride of 1 to extract the features of $16 \times 512 \times 512$ from the input X-ray image of $1 \times 1024 \times 1024$. The second 2D convolutional layer applies 3×3 kernels and a stride of 1 to extract the features of $1 \times 256 \times 256$ from the input X-ray image of $16 \times 512 \times 512$. The image reconstruction part (i.e., decoder) consists of two transposed 2D convolutional layers. The first transposed 2D convolutional layer applies 2×2 kernels and a stride of 2 to reconstruct the features of $16 \times 512 \times 512$ from the features of $1 \times 256 \times 256$. The second transposed 2D convolutional layer applies 2×2 kernels and a stride of 2 to reconstruct the features of $1 \times 1024 \times 1024$ from the features of $16 \times 512 \times 512$. Our model design intends to let the deblurring model understand the key features of objects observed in blurry X-ray images. The original X-ray image of $3{,}012 \times 3{,}012$ is resized to $1{,}024 \times 1{,}024$ to be used for the proposed deblurring model.

2) TRAINING A MODEL

Training a model consists of three main phases. The first phase is the forward pass. This phase is a process of performing a series of calculations based on the learned weight of the model. The encoder extracts features in the form of $1 \times 256 \times 256$ by applying two 2D convolutional layers from a $1 \times 1024 \times 1024$ input image. The decoder reconstructs a $1 \times 1024 \times 1024$ image by applying two transposed 2D convolutional layers to the extracted features.

The second phase compares the output obtained through the forward pass with the desired output (i.e., the input image) to calculate the loss to be used for model training. In our study, the loss between the two images is calculated based on the structural similarity index measure (SSIM). SSIM is a method of comparing the similarity of two images using three elements: luminance, contrast, and structure. SSIM has a value of 0 to 1, and the closer the two images are, the closer the SSIM value is to 1. Because model training is done by decreasing the loss in typical deep learning algorithms, the loss for training a model in our research is as follows:

$$\begin{aligned}&\text{SSIM\_loss}\\&\quad = -SSIM(\text{input image, reconstructed image})\end{aligned} \tag{1}$$

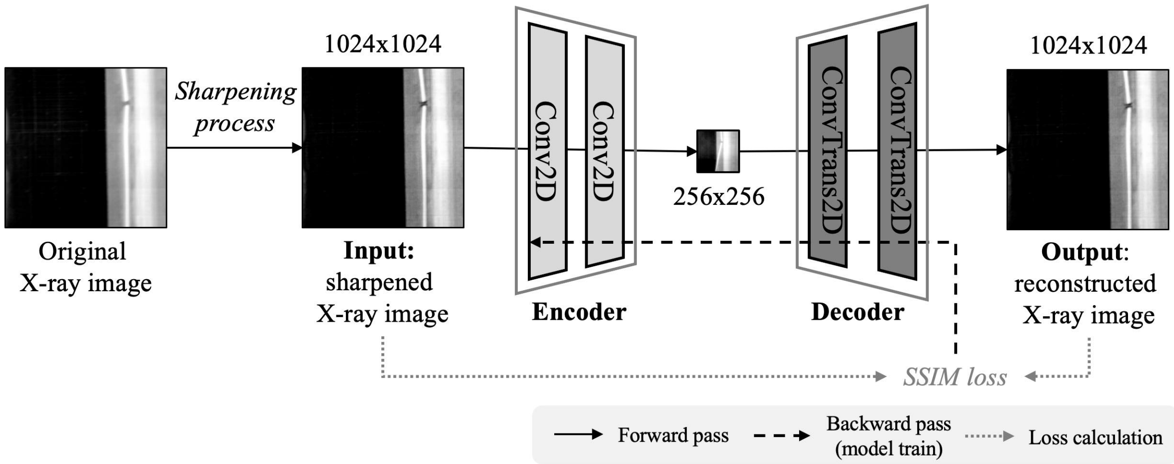

FIGURE 9. The proposed deblurring model and training phase.

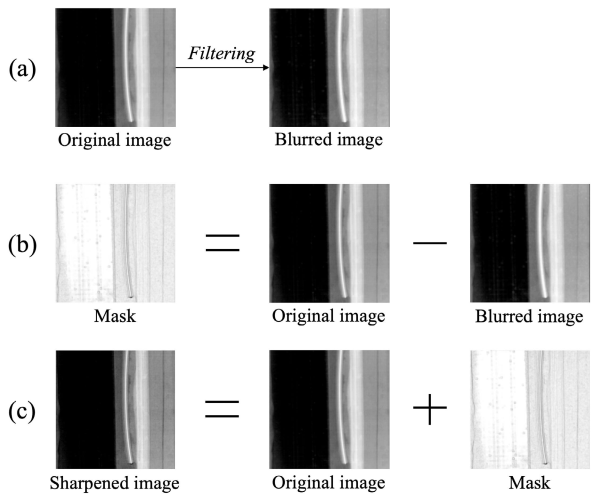

FIGURE 10. Processes of unsharp masking.

The final phase of model training is to update the weight of each part of the model based on the calculated loss. How much weight of each layer constituting the model should be updated is derived by applying the back-propagation technique to the calculated loss. The learning of the model proceeds by updating the weight by the amount derived from the calculated loss.

In realizing unsupervised learning, we do not use the original X-ray images directly. We empirically found that the original blurry X-ray images are not enough for the deep learning model to learn the key features of objects. We conjecture that blurry pixels hinder the deep learning model from learning the features. Instead, we apply unsharp masking to the original X-ray images and then use the sharpened images as inputs to the deep learning model. In our work, all X-ray images (i.e., 1,968 images) are used for training a model.

3) DEBLURRING WITH A TRAINED MODEL

The gist of the proposed method is how to utilize the trained model. Our idea is to apply unsharp masking to the output of the trained encoder, i.e., in latent space. The feature processed in latent space is used as a decoder input, and deblurring is performed through reconstruction. The autoencoder learns key features in reconstructing X-ray images through the training process, especially in expressing objects of interest included in the images. In this process, unnecessary elements, especially blur, are weakened to some extent in latent space. Therefore, we intend to improve the performance of deblurring by applying unsharp masking in latent space where blur is weakened to some extent.

To explain the structure of the autoencoder for deblurring from another aspect, the encoder functions as a downsampler that reduces the size of the input image, and the decoder functions as an upsampler that expands the size of the input image. We intended this when we designed the model. During the downsampling process of the encoder, the degree of blur is weakened, which can be understood as a case where an image gets clearer when its size is reduced. In the process of restoring to its original size after downsampling, the blur effect commonly occurs. We tried to solve this problem by training the decoder to restore its original image without loss. In other words, after downsampling to reduce the degree of blur, unsharp masking is performed, and upsampling without loss is performed on the image to improve deblurring performance compared to unsharp masking in the original space.

D. EXPERIMENTAL RESULTS

A common way to measure deblurring performance is to compare a deblurred image with a corresponding clear image. The more similar the two images, the better the deblurring performance. However, in this research, there are only blurry images, so a performance measurement

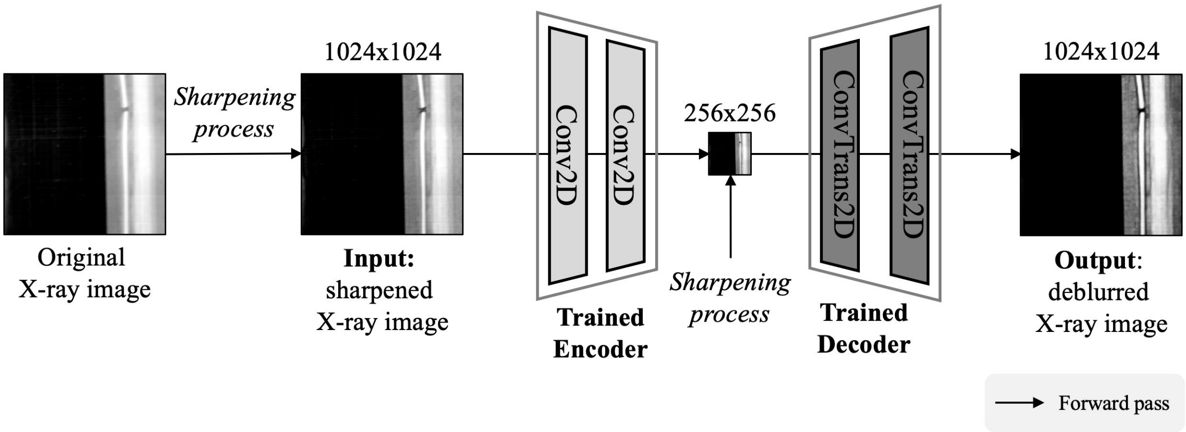

FIGURE 11. Deblurring process with a trained model.

method based on clear images cannot be applied. To measure deblurring performance based only on blurry images (just for performance study), we propose a method using unsharp masking. The idea is to compare an image with the image processed by unsharp masking. The more blurry the image, the more room for improvement through unsharp masking, so there will be a large difference between the original image and the processed image. Therefore, the SSIM value between the original image and the processed image is used as a sharpness metric:

$$\begin{aligned}&\text{Sharpness metric}\\&\quad = SSIM(\text{an image, an image with unsharp masking})\end{aligned} \tag{2}$$

For example, the clearer the image, the less room for improvement through unsharp masking, so the original image and the processed image will be similar, in which case a high SSIM value will be derived. To verify the feasibility of the proposed sharpness metric, the proposed sharpness metric is applied to the original blurry X-ray images and the X-ray images processed by unsharp masking. As a result, using all X-ray images, the average sharpness metric for the original X-ray images is 0.1718, and for the X-ray images processed by unsharp masking is 0.8513. This result shows that the proposed sharpness metric for calculating the sharpness is a somewhat useful way.

Based on the proposed sharpness metric, the methods of unsharp masking in the original space and unsharp masking in the latent space (i.e., the proposed method) are compared. For this, we consider all X-ray images as test images. The average sharpness metrics of the two methods are 0.8513 and 0.8517, respectively, showing no significant difference. We further analyze to confirm that deblurring performance is improved in some cases through the proposed method, and in some cases not. For 41.5% of the images, compared to the unsharp masking in the original space, the proposed method improves the deblurring performance by an average of 0.024 and a maximum of 0.16. Please note that the maximum value of the sharpness metric (i.e., SSIM) is 1. Fig. 12 shows some examples of the improvement by the proposed method. On the contrary, for 58.5% of the images, the proposed method degrades the deblurring performance by an average of 0.016 and a maximum of 0.07. Fig. 13 shows some examples of the degradation by the proposed method. Although there are fewer cases of performance improvement by the proposed method than there are other cases, it can be seen that the degree of performance improvement is greater than the degradation. From the images shown in Fig. 12 and Fig. 13, it can be seen that both methods (i.e., unsharp masking in original space and unsharp masking in latent space) conduct deblurring the images to generate clearer images compared to the original image.

Please note that the sharpness metric does not provide an absolute criterion for measuring the performance of a deblurring model. The sharpness metric was temporarily designed and used in this paper to analyze the performance of the proposed method in an environment where no clear X-ray images correspond to blurry X-ray images. In an environment where there are no clear X-ray images, any sharpness metrics including the metric proposed in this paper cannot be used as a criterion for measuring the performance of a particular deblurring method. The more important thing in evaluating a deblurring model qualitatively is to see whether the pursuit through deblurring has been well achieved. In this paper, our goal of the deblurring process is to make the objects of interest in the image clearer and more prominent. From this perspective, in the case of the proposed method, it can be seen that the contrast between white and black is clearer and the edge is clearer than the method in the original space as shown in Fig. 12 and Fig. 13.

E. DISCUSSION

One of the main purposes of image deblurring is to improve the object detection-based diagnosis. However, the purpose of the image deblurring is not limited to pre-processing for object detection. The image deblurring is also required for other purposes like increasing the readability of the human operator. At the time of conducting our study of image deblurring on the testbed, we expected a blur effect

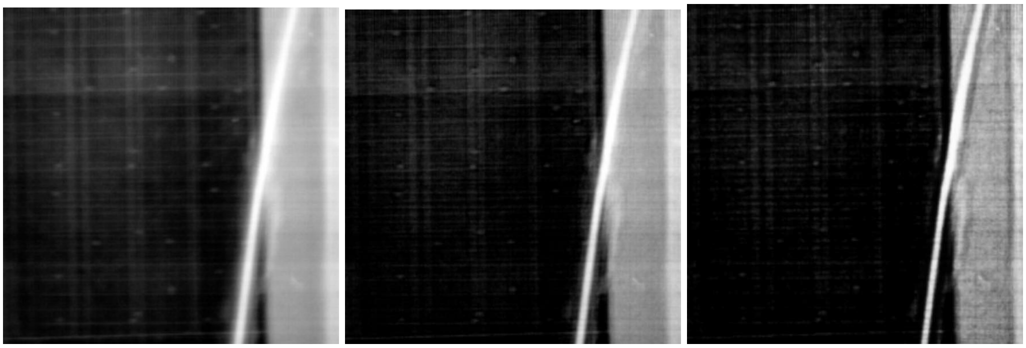

(a) Example1: original X-ray image (0.0003).
(b) Example1: sharpening in original space (0.6987).
(c) Example1: sharpening in latent space (**0.8316**).

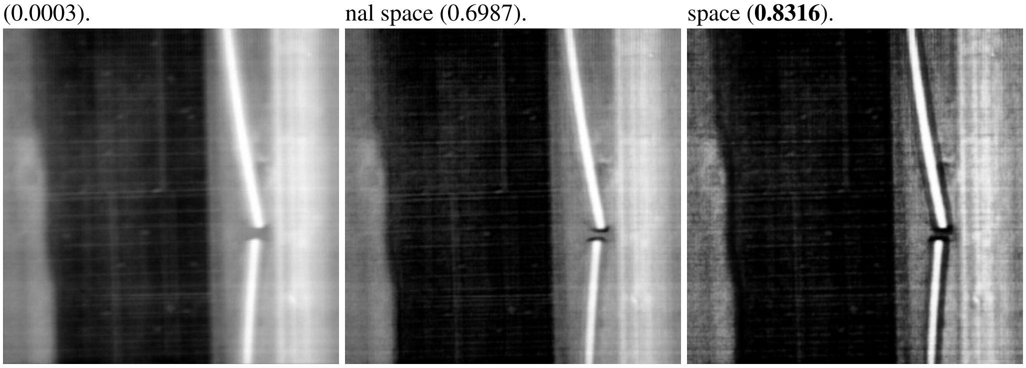

(d) Example2: original X-ray image (0.00008).
(e) Example2: sharpening in original space (0.7134).
(f) Example2: sharpening in latent space (**0.7916**).

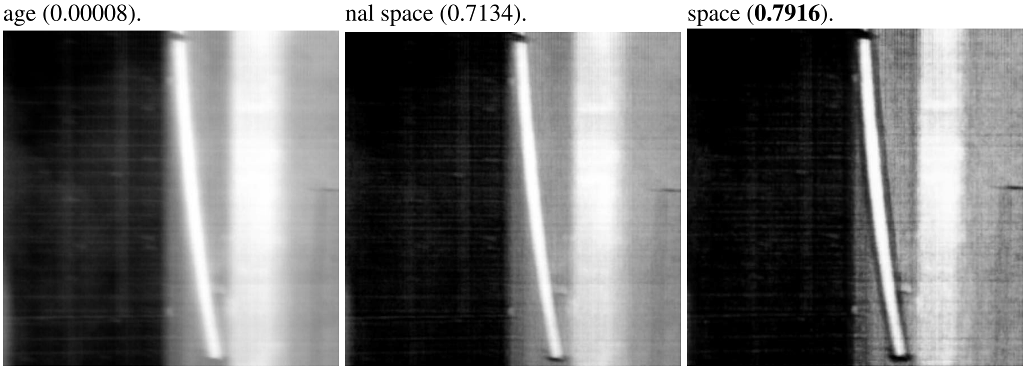

(g) Example3: original X-ray image (0.0137).
(h) Example3: sharpening in original space (0.7627).
(i) Example3: sharpening in latent space (**0.842**).

FIGURE 12. Comparison of deblurring methods: case #1. The first column: original X-ray images, the second column: unsharp masking in the original space, and the third column: unsharp masking in the latent space (i.e., the proposed method).

due to the slight movement of the drones and observed the blur effect from the drone-driven X-ray images. Using the X-ray images acquired from the testbed, we conducted image deblurring research for several purposes. However, experiments conducted on the testbed show that the image deblurring did not significantly improve the performance of object detection. We conjecture that the blurry X-ray images themselves contain enough necessary information so that the object detection model has no difficulty in extracting the necessary features. However, this does not mean that image deblurring is not necessary for the object detection-based diagnosis. Please note that we plan to apply our methods to wind turbines in actual operation. We expect that the blur effect gets worse in those environments and thus that the performance improvement by the image deblurring is not marginal. We will continue the image deblurring research to ensure that the object detection-based diagnosis can achieve good performance even in such harsh environments. We may be able to continue a study on the deblurring algorithm by adding an artificial blur effect on the acquired X-ray images. However, we found that the artificial blur is quite far from the blur generated by the drones in real-world applications. Therefore, the deblurring model trained on the X-ray images with the artificial blur may not be useful in an actual environment. Further research on the deblurring algorithm can be conducted only after we acquire new X-ray

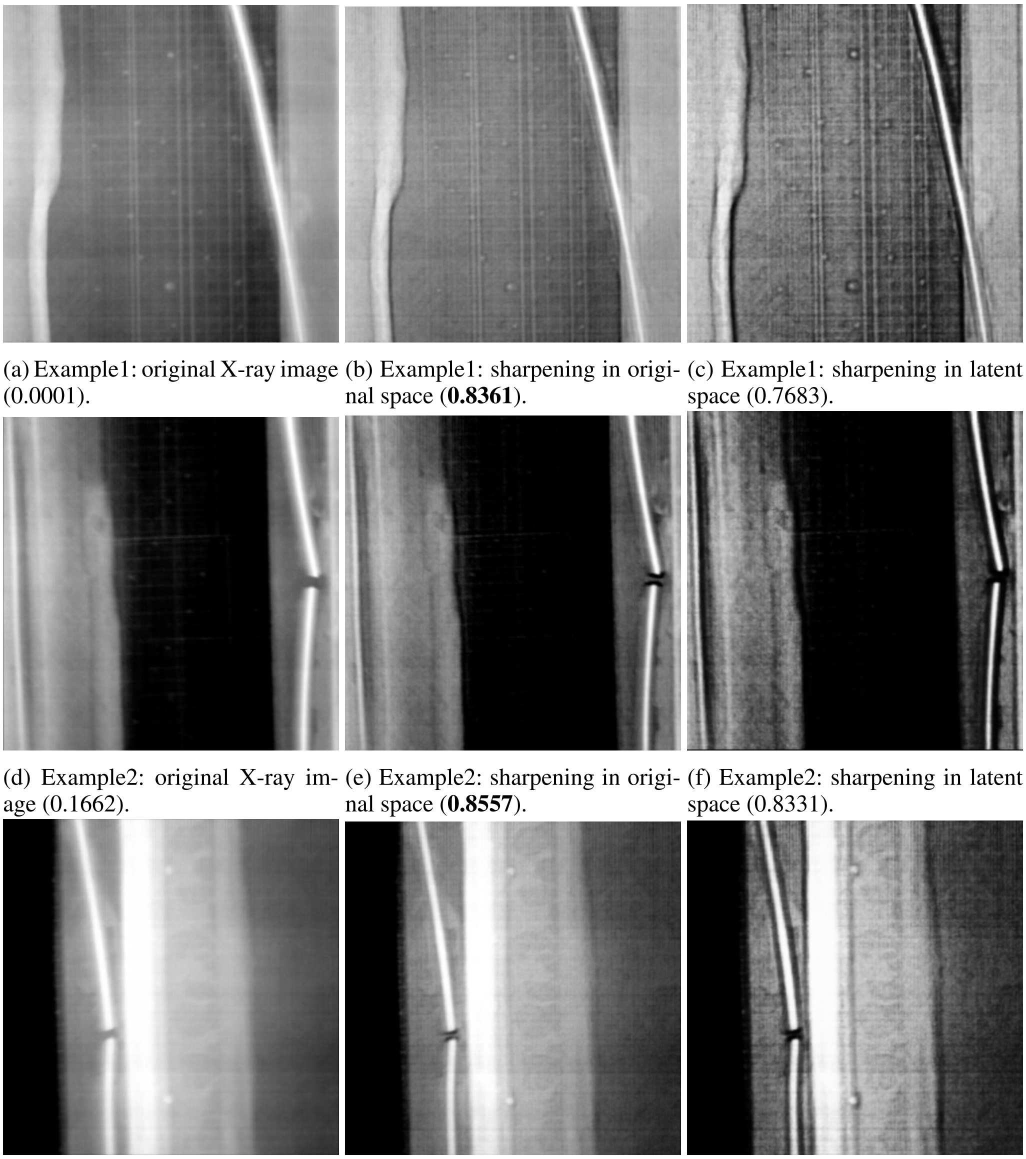

(a) Example1: original X-ray image (0.0001). (b) Example1: sharpening in original space (**0.8361**). (c) Example1: sharpening in latent space (0.7683).

(d) Example2: original X-ray image (0.1662). (e) Example2: sharpening in original space (**0.8557**). (f) Example2: sharpening in latent space (0.8331).

(g) Example3: original X-ray image (0.1517). (h) Example3: sharpening in original space (**0.8558**). (i) Example3: sharpening in latent space (0.8332).

FIGURE 13. Comparison of deblurring methods: case #2. The first column: original X-ray images, the second column: unsharp masking in the original space, and the third column: unsharp masking in the latent space (i.e., the proposed method).

images with greater blur through application in a harsh real field.

V. OBJECT DETECTION-BASED DIAGNOSIS AND CONTROL

A. OBJECTIVE AND CHALLENGING ISSUES

In this research, only X-ray images are used as input to the model. Given an X-ray image, we need to detect the down conductor cable and determine whether there is an abnormality by classifying the detected objects. We also need to determine which direction the drones should move to capture the other part of the down conductor cable. Regarding the drone flight direction determination, we assume that the drones are moved to the starting point for diagnosis manually or autonomously via an autonomous pilot program, which is out of the scope of this paper. In many cases, the down conductor cable is installed from the tip of the blade, so the tip of the blade can be considered as the starting point. It is necessary to determine which direction the drone will move from the starting point. If there is information about the internal structure of the blade, this information and the angle of the blade can be considered to calculate how much it will move from the starting point. In this paper, we consider the case where there is no such information about the internal structure of the blade. Without the information about the internal structure of the blade, it is necessary to determine the

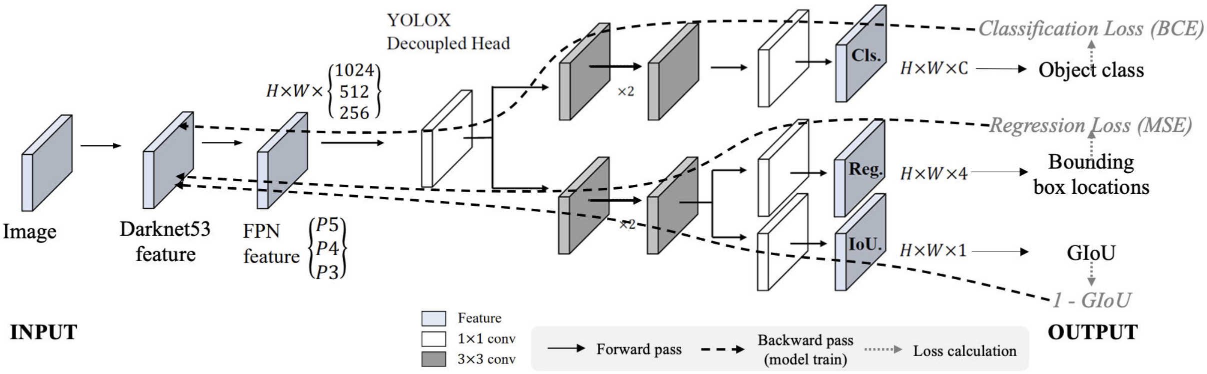

FIGURE 14. YOLOX-Tiny model and training phase.

drone flight direction because the down conductor cable can be installed inside the blade in various shapes. In addition, the blade to be diagnosed can be given at various angles. Therefore, calculating the drone flight direction based on the X-ray image is a key function required for autonomous flight because it determines in which direction the drone should move from the starting point to take X-ray images.

In pursuing the objectives above, we have two challenging issues. First, we need to consider the trade-off between detection performance in accuracy and real-time operability. The drones must wait until the next direction of movement is determined after X-ray imaging. Therefore, the diagnosis process should be as fast as possible to reduce the battery consumption of drones while providing reasonable detection accuracy. Second, possible directions need to be considered in determining the direction of drone movement for the next X-raying.

To realize fast and accurate diagnosis while solving the challenging issues above, we adopt an object detection-based approach using YOLOX-Tiny [36]. Instead of doing classification based on the entire image, we apply a method of detecting objects within the image and classifying the states of each detected object for the following reasons:

- The object detection-based method has the advantage of being able to adjust the drone position so that the object of interest is in the center of the image as needed because we know the position of the objects. On the contrary, it is not easy to identify the location of the object of interest with the image-level classification.
- Adopting the object detection-based method has the advantage of detecting one or more objects and classifying the states of each detected object to enable more accurate diagnosis. In addition, given an image including multiple objects, object detection allows us to know the position of each object within the image. On the contrary, it is very hard to do the same job with image-level classification.
- By adopting the object detection-based method, we can identify which part of the image has an abnormal object. On the contrary, the image-level classification does not do the same job.

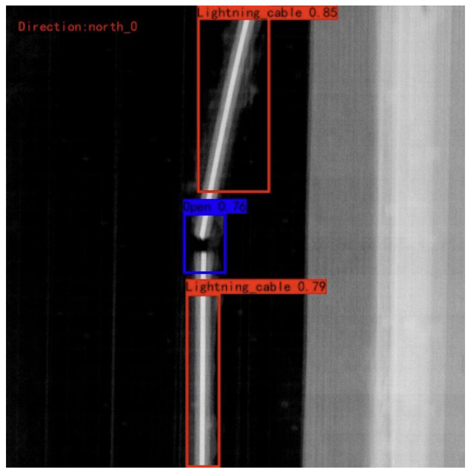

FIGURE 15. An example of object detection results in an X-ray image.

To realize the drone flight direction determination, we apply a rotation-based data augmentation technique to simulate down conductor cables installed in different directions. A detailed description of our methods will be given in the following subsections.

B. BACKGROUNDS: OBJECT DETECTION AND YOLOX-TINY

For a clear presentation, we first briefly introduce object detection and YOLOX-Tiny as a base for our model. Given an image with one or more objects, *object detection* refers to a task that locates the presence of objects with bounding boxes (i.e., object localization) and identifies classes of the detected objects in an image (i.e., object classification). Fig. 15 shows an example of an object detection result. In Fig. 15, rectangular boxes (i.e., bounding boxes) are displayed at the location of the detected objects and the texts above the rectangular boxes show the classification results of the detected objects.

There have been various object detection methods. With the rapid advancement of deep learning, object detection methods rooted in deep learning have gained widespread adoption in the field of computer vision. In 2014, Girshick et al. introduced Regions with convolutional neural

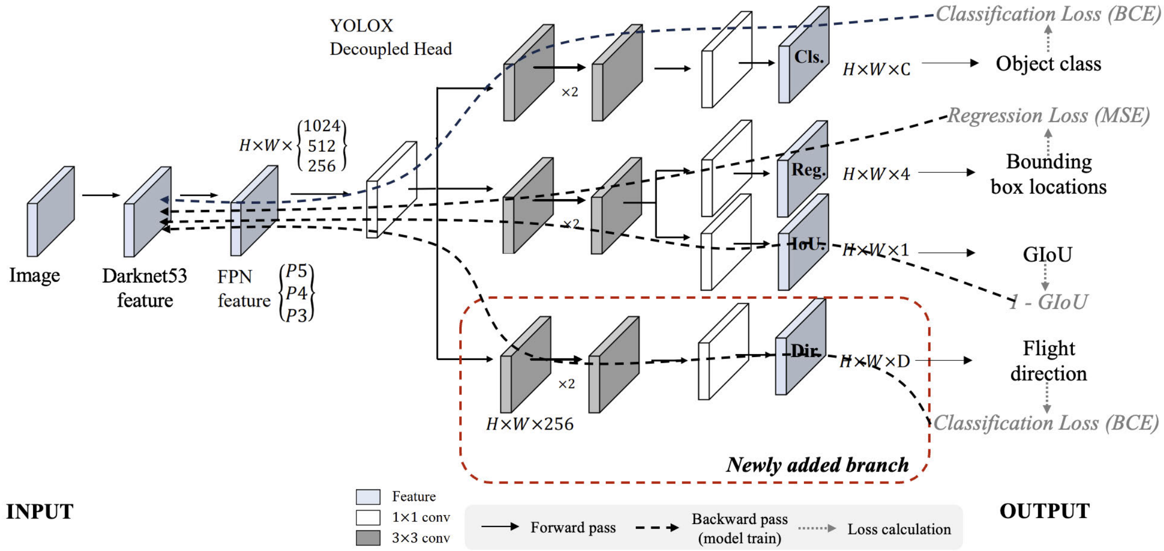

FIGURE 16. Xray-YOLOX-Tiny model and training phase.

network (CNN) features, known as R-CNN, [49], which marked the inception of a two-stage network integrating region proposal and CNNs. Subsequently, in 2015, a faster and more precise iteration of R-CNN, known as Fast R-CNN, was introduced [50]. Building upon this progress, Ren et al. devised the pioneering end-to-end network called Faster-RCNN [51], which was based on the foundation laid by Fast-RCNN. In recent times, single-stage detection networks like RetinaNet (Lin et al., [52]) and the You Only Look Once (YOLO) series (the first YOLO model [53]; YOLO9000 [54]; YOLOv3 [55]; YOLOv4 [56]; YOLOX [36]) have gained prominence due to their superior detection speed.

Among the various models for object detection, we adopt YOLOX algorithm [36] that achieves a significant improvement over other algorithms. YOLOX is divided into X, L, M, S, and Tiny models according to network depth and width for various usage scenarios. Of these branches, YOLOX-Tiny stood out by not only improving detection accuracy but also by shrinking the model size, effectively addressing crucial concerns within the field. Furthermore, YOLOX-Tiny as a one-stage algorithm that bounding boxes of target objects and predicted categories are simultaneously generated has a good balance between high detection precision and high detection speed. Considering the advantages of YOLOX-Tiny mentioned above, we select the lightweight network for real-time object detection, YOLOX-Tiny, as a backbone network to achieve our goal.

Fig. 14 shows a structure of YOLOX-Tiny model. YOLOX-Tiny model allows for variable input image sizes. An input image is processed by the Darknet53 [55] and the feature pyramid network (FPN [57]) to produce 3 feature blocks (i.e., in the shape of HxWx{256,512,1024}). Then, the feature blocks are processed by decoupled heads for classification and regression tasks. Classification and regression results from the 3 feature blocks are aggregated to produce one final classification and regression result. The classification task is about identifying the class of a detected object. The regression task is about finding a bounding box of a detected object (i.e., 4 points). Another output of the regression task is generalized intersection over union (GIoU), calculated using the predicted bounding box and the corresponding true bounding box. If the prediction of a bounding box is perfectly accurate, GIoU would be 1. Train loss consists of the classification loss, the regression loss, and the localization (i.e., GIoU) loss [58] as follows:

$$\begin{aligned} &\text{YOLOX} - \text{Tiny\_loss} \\ &\quad = BCE(\text{pred. object class, true object class}) \\ &\qquad + MSE(\text{pred. bounding box, true bounding box}) \\ &\qquad + (1 - GIoU), \end{aligned} \tag{3}$$

where BCE and MSE indicate binary cross entropy and mean squared error, respectively. Because training a model tries to minimize the loss, (1 - GIoU) is used rather than GIoU.

C. PROPOSED ARCHITECTURE: XRAY-YOLOX-TINY

We propose an improved YOLOX-Tiny, named *Xray-YOLOX-Tiny*, for 1) object detection and 2) classification of the direction of the detected object in the X-ray images. Fig. 16 shows an architecture of Xray-YOLOX-Tiny model. YOLOX-Tiny shows good detection performance when we tested the trained model with the X-ray images of the wind turbine blade. However, the base model only provides the function to determine the location and class of the objects and does not provide the function to determine the direction of the object, which is required for controlling the drones. To realize the additional requirement for our purpose, we developed Xray-YOLOX-Tiny by adding a branch network for direction classification to YOLOX-Tiny model. The purpose of the newly added branch network is to

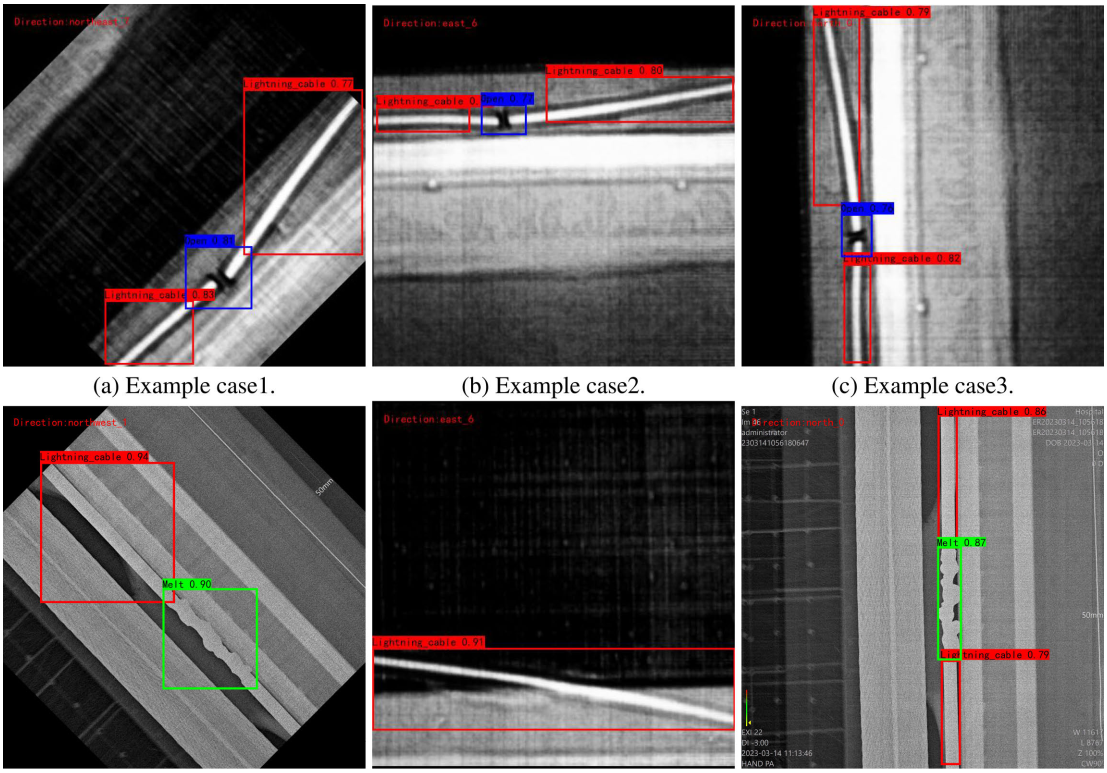

(a) Example case1. (b) Example case2. (c) Example case3.

(d) Example case4. (e) Example case5. (f) Example case6.

FIGURE 17. Examples of object detection results by Xray-YOLOX-Tiny.

provide a direction determination function as classification by physically combining the conventional two branches known as decoupled heads. The new branch utilizes the feature blocks extracted from the FPN as stem features. After undergoing several rounds of dimension reduction from each stem feature, the direction scores for eight possible directions are derived to classify the entire image as a single direction, instead of focusing on bounding boxes. The classification probabilities are finally computed by a softmax layer with the direction scores averaged over all the extracted features. The training loss of Xray-YOLOX-Tiny is as follows:

$$\begin{aligned}
&\text{Xray} - \text{YOLOX-Tiny_loss} \\
&\quad = BCE(\text{pred. object class, true object class}) \\
&\qquad + MSE(\text{pred. bounding box, true bounding box}) \\
&\qquad + (1 - GIoU) \\
&\qquad + BCE(\text{pred. direction class, true direction class}). \qquad (4)
\end{aligned}$$

The regression loss (in MSE) and the localization loss (in 1 – GIoU) are for object localization. The binary cross entropy (in BCE) is for the object classification.

D. EXPERIMENTAL RESULTS

From the perspective of object detection, the dataset for training and testing includes three objects, a regular down conductor cable (i.e., Lightning cable), and two abnormal defects (i.e., Melt and Open). For the drone flight direction determination, the dataset is augmented by rotating X-ray images into eight direction classes (i.e., north, northwest, west, southwest, south, southeast, east, and northeast). The proposed model is trained at 320 × 320 resolution images (i.e., resized images from the original X-ray images), with 300 epochs on a Tesla V100 GPU. The number of training images is 1,817 and the number of test images is 151. Lightning cable, Melt, and Open images are distributed evenly across the training and test datasets according to their size.

Fig. 17 shows some results of object detection by Xray-YOLOX-Tiny. A detection result includes a bounding box, a class name, a confidence score for each detected object, and a flight direction for an image. In each bounding box, the class name of the detected object and the probability are indicated. In many cases, objects are detected with probability values of 0.8 or higher. The direction classification results are displayed in the upper left corner of the image. The classification results are expressed in numbers from 0 to 7, with 0 to 7 representing North, Northwest, West, Southwest, South, Southwest, East, and Northeast, respectively. Adopting an object detection-based method, our method accurately identifies which part of the image has an abnormal object.

Table 1 shows the performance of object detection by Xray-YOLOX-Tiny. Object detection performance can be analyzed in terms of object localization (i.e., estimating the location of the bounding boxes) and object classification (i.e., estimating the class of objects in the bounding boxes). The bounding box estimation is handled as a regression

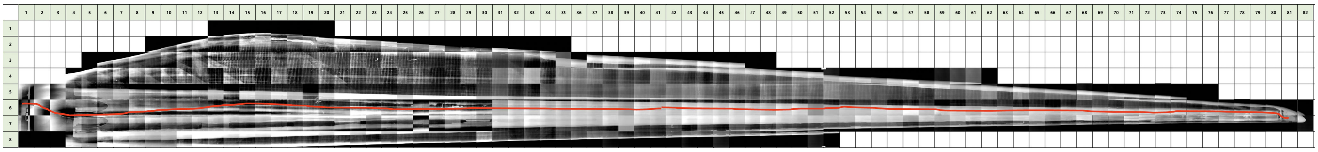

FIGURE 18. X-ray images of a 65-meter-long wind turbine blade (stitched from separate X-ray image). The red line indicates the down conductor cable.

TABLE 1. Performance of object detection by Xray-YOLOX-Tiny.

Class		Regression AP (%)	Object Classification F1 score	Recall (%)	Precision (%)	AUC
Normal	Lightning cable	99.19	0.99	98.03	99.13	-
Abnormal	Melt	99.98	0.99	98.74	99.37	
	Open	95.48	0.96	93.98	97.45	
	All	98.21 (mAP)	0.98	96.91	98.29	0.903

TABLE 2. Performance comparison of YOLOX-Tiny and Xray-YOLOX-Tiny.

Method	Params	Regression (mAP)	Classification (AUC) Object	Direction	Latency (ms)
YOLOX-Tiny	9.0M	98.35	0.903	N/A	14.32
Xray-YOLOX-Tiny	11.2M	98.21	0.901	0.999	16.70

task, and thus the performance is typically calculated as average precision (AP in %) for each object class or mAP across all classes. AP for Lightning cable, Melt, and Open are 99.19%, 99.98%, and 95.48%, respectively. mAP across all classes is 98.21%. The performance of the object classification problem is usually calculated by F1 score, Recall (in %), Precision (in %), and AUC. F1 score of the object classification is 0.99, 0.99, and 0.96 in Lightning cable, Melt, and Open, achieving an average performance of 0.98. Recall of the object classification is 98.03%, 98.74%, and 93.98% in the case of Lighting cable, Melt, and Open, achieving an average performance of 96.91%. Precision of the object classification is 99.13%, 99.37%, and 97.45% in Lightning cable, Melt, and Open, achieving an average performance of 98.29%. AUC of the object classification across all classes is 0.903. The above results show that the proposed Xray-YOLOX-Tiny exhibits good performance in object localization and classification in wind turbine blade X-ray images.

Table 2 compares YOLOX-Tiny and Xray-YOLOX-Tiny. Xray-YOLOX-Tiny shows a slightly larger number of parameters than YOLOX-Tiny due to the network added for the direction classification. Xray-YOLOX-Tiny has 11.2M parameters, while YOLOX-Tiny has 9M parameters. In the regression performance for finding bounding box locations, the two models perform similar performances. YOLOX-Tiny shows 98.35% and Xray-YOLOX-Tiny shows 98.21% in mAP. In terms of object classification, YOLOX-Tiny shows an AUC of 0.903 and Xray-YOLOX-Tiny shows an AUC of 0.901, achieving similar performance. On the other hand, YOLOX-Tiny does not provide drone flight direction classification, but Xray-YOLOX-Tiny achieves an AUC of 0.999 in terms of drone flight direction classification. In particular, F1, Precision, Recall for all eight directions are 0.99, 99.9%, and 99.9%. The execution time of Xray-YOLOX-Tiny is slightly increased compared to YOLOX-Tiny. Xray-YOLOX-Tiny shows an average runtime of 16.7 ms, an increase of 2.38 ms from 14.32 ms on YOLOX-Tiny. The above results show that Xray-YOLOX-Tiny can support drone direction classification while sustaining the object detection performance with a slight increase in the number of parameters and execution time over YOLOX-Tiny.

E. DISCUSSION

The primary interest of our current research is to diagnose a down conductor cable installed inside the blade. However, we plan to expand the diagnosis target to various cases inside and outside the blade (e.g., cracks, holes, and so on). One of the goals of our current research is to conduct a diagnosis using a separate X-ray image. An expert needs to finally diagnose the state of the down conductor cable using all X-ray images of the whole down conductor cable. For example, given a 65-meter-long blade, it is expected to take about 82 X-ray images to see the whole down conductor cable (Fig. 18). In other words, the purpose of current research is to help experts perform the final diagnosis by providing pre-diagnosis results of each part of the down conductor cable.

VI. CONCLUSION

For stable operation of wind turbines, continuous diagnosis of the main parts of the wind turbines is necessary. For efficient diagnosis, it is necessary not only to secure the accuracy of diagnosis but also to reduce the time and cost required for diagnosis. This paper proposes technologies for efficient diagnosis of down conductor cables inside wind blades. We propose an unsupervised deblurring model for blurry X-ray images taken by two synchronized drones. We also propose a model for object detection (i.e., diagnosis) and flight direction determination (for guiding the drones for further X-ray imaging) using the deblurred X-ray images. Through experiments using the X-ray images taken by drones, we verify the feasibility of our proposed models. As future work, we plan to improve the proposed methods by applying them to the wind turbines in actual operation. In particular, we plan to apply our methods to 4.3MW and 2MW-class wind turbines installed near the sea, which is considered an appropriate place to examine and improve the proposed methods through trial and error with difficult wind speeds and directions.

REFERENCES

[1] *GHG Reduction Programs & Strategies*. [Online]. Available: https://www.epa.gov/climateleadership/ghg-reduction-programs-strategies/

[2] *What is Carbon Neutrality and How Can it Be Achieved by 2050*. [Online]. Available: https://www.europarl.europa.eu/news/en/headlines/society/20190926STO62270/what-is-carbon-neutrality-and-how-can-it-be-achieved-by-2050/.

[3] *Electricity Mix*. [Online]. Available: https://ourworldindata.org/electricity-mix/

[4] (2023). *Global Wind Report 2023*. [Online]. Available: https://gwec.net/wp-content/uploads/2023/03/GWR-2023_interactive.pdf/

[5] *Wind Turbines: The Bigger, the Better*. [Online]. Available: https://www.energy.gov/eere/articles/wind-turbines-bigger-better/

[6] (2023). *Land-Based Wind Market Report: 2023 Edition*. [Online]. Available: https://www.energy.gov/ere/wind/articles/land-based-wind-market-report-2023-edition/

[7] *IEC 61400-24*. [Online]. Available: https://webstore.iec.ch/preview/info_iec61400-24%7Bed2.0%7Den.pdf/

[8] M. Civera and C. Surace, "Non-destructive techniques for the condition and structural health monitoring of wind turbines: A literature review of the last 20 years," *Sensors*, vol. 22, no. 4, p. 1627, Feb. 2022.

[9] L. Wang, Z. Zhang, and X. Luo, "A two-stage data-driven approach for image-based wind turbine blade crack inspections," *IEEE/ASME Trans. Mechatronics*, vol. 24, no. 3, pp. 1271–1281, Jun. 2019.

[10] J. Gu, G. Liu, and M. Li, "Damage detection for rotating blades using digital image correlation with an AC-SURF matching algorithm," *Sensors*, vol. 22, no. 21, p. 8110, Oct. 2022.

[11] A. Shihavuddin, X. Chen, V. Fedorov, A. N. Christensen, N. A. B. Riis, K. Branner, A. B. Dahl, and R. R. Paulsen, "Wind turbine surface damage detection by deep learning aided drone inspection analysis," *Energies*, vol. 12, no. 4, p. 676, Feb. 2019.

[12] X. Yang, Y. Zhang, W. Lv, and D. Wang, "Image recognition of wind turbine blade damage based on a deep learning model with transfer learning and an ensemble learning classifier," *Renew. Energy*, vol. 163, pp. 386–397, Jan. 2021.

[13] A. Reddy, V. Indragandhi, L. Ravi, and V. Subramaniyaswamy, "Detection of cracks and damage in wind turbine blades using artificial intelligence-based image analytics," *Measurement*, vol. 147, Dec. 2019, Art. no. 106823.

[14] X.-Y. Zhao, C.-Y. Dong, P. Zhou, M.-J. Zhu, J.-W. Ren, and X.-Y. Chen, "Detecting surface defects of wind tubine blades using an alexnet deep learning algorithm," *IEICE Trans. Fundam. Electron., Commun. Comput. Sci.*, vol. E102.A, no. 12, pp. 1817–1824, Dec. 2019.

[15] D. Sarkar and S. K. Gunturi, "Wind turbine blade structural state evaluation by hybrid object detector relying on deep learning models," *J. Ambient Intell. Humanized Comput.*, vol. 12, no. 8, pp. 8535–8548, Oct. 2020.

[16] Z. Qiu, S. Wang, Z. Zeng, and D. Yu, "Automatic visual defects inspection of wind turbine blades via YOLO-based small object detection approach," *J. Electron. Imag.*, vol. 28, no. 4, p. 1, Aug. 2019.

[17] R. Wu, D. Zhang, Q. Yu, Y. Jiang, and D. Arola, "Health monitoring of wind turbine blades in operation using three-dimensional digital image correlation," *Mech. Syst. Signal Process.*, vol. 130, pp. 470–483, Sep. 2019.

[18] J. Curt, M. Capaldo, F. Hild, and S. Roux, "Modal analysis of a wind turbine tower by digital image correlation," *J. Phys., Conf. Ser.*, vol. 1618, no. 2, Sep. 2020, Art. no. 022002.

[19] A. A. Jiménez, F. P. G. Márquez, V. B. Moraleda, and C. Q. Gómez Muñoz, "Linear and nonlinear features and machine learning for wind turbine blade ice detection and diagnosis," *Renew. Energy*, vol. 132, pp. 1034–1048, Mar. 2019.

[20] P. Wang, W. Zhou, Y. Bao, and H. Li, "Ice monitoring of a full-scale wind turbine blade using ultrasonic guided waves under varying temperature conditions," *Struct. Control Health Monitor.*, vol. 25, no. 4, p. e2138, Jan. 2018.

[21] N. Zhang, W. Bian, and B. Pan, "The application of ultrasonic phased array technology in wind turbine blade defect detection system," *IOP Conf. Ser., Earth Environ. Sci.*, vol. 675, no. 1, Feb. 2021, Art. no. 012077.

[22] G. Nicholas, "Development of novel ultrasonic monitoring techniques for improving the reliability of wind turbine gearboxes," Ph.D. thesis, Univ. Sheffield, Sheffield, U.K., Feb. 2021, vol. 132.

[23] P. Liu, D. Xu, J. Li, Z. Chen, S. Wang, J. Leng, R. Zhu, L. Jiao, W. Liu, and Z. Li, "Damage mode identification of composite wind turbine blade under accelerated fatigue loads using acoustic emission and machine learning," *Structural Health Monitor.*, vol. 19, no. 4, pp. 1092–1103, Jul. 2020.

[24] Y. Zhang, Y. Cui, Y. Xue, and Y. Liu, "Modeling and measurement study for wind turbine blade trailing edge cracking acoustical detection," *IEEE Access*, vol. 8, pp. 105094–105103, 2020.

[25] M. Inalpolat and C. Niezrecki, "Acoustic sensing based operational monitoring of wind turbine blades," *J. Phys., Conf. Ser.*, vol. 1452, no. 1, Jan. 2020, Art. no. 012050.

[26] C. Traylor, M. DiPaola, D. J. Willis, and M. Inalpolat, "A computational investigation of airfoil aeroacoustics for structural health monitoring of wind turbine blades," *Wind Energy*, vol. 23, no. 3, pp. 795–809, Mar. 2020.

[27] D. Xu, P. F. Liu, Z. P. Chen, J. X. Leng, and L. Jiao, "Achieving robust damage mode identification of adhesive composite joints for wind turbine blade using acoustic emission and machine learning," *Compos. Struct.*, vol. 236, Mar. 2020, Art. no. 111840.

[28] J. Solimine, C. Niezrecki, and M. Inalpolat, "An experimental investigation into passive acoustic damage detection for structural health monitoring of wind turbine blades," *Struct. Health Monitor.*, vol. 19, no. 6, pp. 1711–1725, Jan. 2020.

[29] B. Chen, S. Yu, Y. Yu, and Y. Zhou, "Acoustical damage detection of wind turbine blade using the improved incremental support vector data description," *Renew. Energy*, vol. 156, pp. 548–557, Aug. 2020.

[30] S. Ding, C. Yang, and S. Zhang, "Acoustic-signal-based damage detection of wind turbine blades—A review," *Sensors*, vol. 23, pp. 1–23, May 2023.

[31] H. Hassan and T. N. Tallman, "Experimental identification of stress concentrations in piezoresistive nanocomposites via electrical impedance tomography," in *Proc. Sensors Smart Struct. Technol. Civil, Mech., Aerosp. Syst.*, Mar. 2019, pp. 380–388.

[32] L. Mishnaevsky, S.Fster, L.P. Mikkelsen, Y. Kusano, and J.I. Bech, "Micromechanisms of leading edge erosion of wind turbine blades: X-ray tomography analysis and computational studies," *Wind Energy*, vol. 23, pp. 547–563, Mar. 2020.

[33] S. Zheng, Z. Yifeng, P. Xiao, and W. Peng, "Dimensional reduction analyzing the thermoelastic behavior of wind turbine blades based on the variational asymptotic multiscale method," *Compos. Struct.*, vol. 254, Dec. 2020, Art. no. 112835.

[34] A. Khadka, Y. Dong, and J. Baqersad, "Structural health monitoring of wind turbines using a digital image correlation system on a UAV," in *Proc. Conf. Soc. Exp. Mech. Ser. ((CPSEMS))*, vol. 6, Apr. 2019, pp. 85–91.

[35] J. Franko, S. Du, S. Kallweit, E. Duelberg, and H. Engemann, "Design of a multi-robot system for wind turbine maintenance," *Energies*, vol. 13, no. 10, p. 2552, May 2020.

[36] Z. Ge, S. Liu, F. Wang, Z. Li, and J. Sun, "YOLOX: Exceeding YOLO series in 2021," 2021, *arXiv:2107.08430*.

[37] A. S. Ayub, W. H. Siew, and S. J. MacGregor, "External lightning protection system for wind turbine blades— Preliminary aerodynamic results," in *Proc. Int. Conf. Lightning Protection (ICLP)*, Oct. 2014, pp. 386–391.

[38] A. Candela Garolera, S. F. Madsen, M. Nissim, J. D. Myers, and J. Holboell, "Lightning damage to wind turbine blades from wind farms in the U.S.," *IEEE Trans. Power Del.*, vol. 31, no. 3, pp. 1043–1049, Jun. 2016.

[39] B. M. Radičević, M. S. Savić, S. F. Madsen, and I. Badea, "Impact of wind turbine blade rotation on the lightning strike incidence—A theoretical and experimental study using a reduced-size model," *Energy*, vol. 45, no. 1, pp. 644–654, Sep. 2012.

[40] *SpectX*. [Online]. Available: https://spectx.nl/

[41] (2023). *Grant-Funded Project SpectX Revolutionizes Offshore Turbine Inspection*. [Online]. Available: https://windpowernl.com/2023/05/22/grant-funded-project-spectx-revolutionizes-offshore-turbine-inspection/.

[42] R. B. Langley, "RTK GPS," *GPS World*, vol. 9, no. 9, pp. 70–76, 1998.

[43] L. Meier, J. Camacho, B. Godbolt, J. Goppert, L. Heng and M. Lizarraga. (2012). *MAVLink: Micro Air Vehicle Communication Protocol*. [Online]. Available: http://qgroundcontrol.org/mavlink/start/

[44] N. Triruttanapiruk, K. Yamamoto, S. Sumi, S. Yokoyama, and K. Obayashi, "Practical use of detection techniques for down conductor disconnections in wind turbine blades," *Electr. Power Syst. Res.*, vol. 187, Oct. 2020, Art. no. 106516.

[45] N. Triruttanapiruk, I. Kodera, and K. Yamamoto, "Approach techniques for detecting disconnected locations of down conductors inside wind turbine blades without trial and error," in *Proc. 34th Int. Conf. Lightning Protection (ICLP)*, Sep. 2018, pp. 1–5.

[46] N. Triruttanapiruk and K. Yamamoto, "Application of genetic algorithm to detect disconnected locations of down conductors along wind turbine blades," in *Proc. 11th Asia–Pacific Int. Conf. Lightning (APL)*, Jun. 2019, pp. 1–4.

[47] N. Triruttanapiruk, K. Yamamoto, S. Sumi, and S. Yokoyama, "A simplified technique for detecting disconnections along down conductors in wind turbine blades," *Electric Power Syst. Res.*, vol. 172, pp. 177–182, Jul. 2019.

[48] C.-F. W. R. Kikinis and H. Knutsson, *Handbook of Medical Imaging: Adaptive Image Filtering*, 2000.

[49] R. Girshick, J. Donahue, T. Darrell, and J. Malik, "Rich feature hierarchies for accurate object detection and semantic segmentation," in *Proc. IEEE Conf. Comput. Vis. Pattern Recognit.*, Jun. 2014, pp. 580–587.

[50] R. Girshick, "Fast R-CNN," in *Proc. IEEE Int. Conf. Comput. Vis. (ICCV)*, Dec. 2015, pp. 1440–1448.

[51] S. Ren, K. He, R. Girshick, and J. Sun, "Faster R-CNN: Towards real-time object detection with region proposal networks," *IEEE Trans. Pattern Anal. Mach. Intell.*, vol. 39, no. 6, pp. 1137–1149, Jun. 2017.

[52] T.-Y. Lin, P. Goyal, R. Girshick, K. He, and P. Dollár, "Focal loss for dense object detection," in *Proc. IEEE Int. Conf. Comput. Vis. (ICCV)*, Oct. 2017, pp. 2999–3007.

[53] J. Redmon, S. Divvala, R. Girshick, and A. Farhadi, "You only look once: Unified, real-time object detection," in *Proc. IEEE Conf. Comput. Vis. Pattern Recognit. (CVPR)*, Jun. 2016, pp. 779–788.

[54] J. Redmon and A. Farhadi, "YOLO9000: Better, faster, stronger," in *Proc. IEEE Conf. Comput. Vis. Pattern Recognit. (CVPR)*, Honolulu, HI, USA, Jul. 2017, pp. 7263–7271.

[55] J. Redmon and A. Farhadi, "YOLOv3: An incremental improvement," 2018, *arXiv:1804.02767*.

[56] A. Bochkovskiy, C.-Y. Wang, and H.-Y. M. Liao, "YOLOv4: Optimal speed and accuracy of object detection," 2020, *arXiv:2004.10934*.

[57] T.-Y. Lin, P. Dollár, R. Girshick, K. He, B. Hariharan, and S. Belongie, "Feature pyramid networks for object detection," in *Proc. IEEE Conf. Comput. Vis. Pattern Recognit. (CVPR)*, Jul. 2017, pp. 936–944.

[58] H. Rezatofighi, N. Tsoi, J. Gwak, A. Sadeghian, I. Reid, and S. Savarese, "Generalized intersection over union: A metric and a loss for bounding box regression," in *Proc. IEEE/CVF Conf. Comput. Vis. Pattern Recognit. (CVPR)*, Jun. 2019, pp. 658–666.

HYUNYONG LEE received the B.S. degree in computer science from Chonnam National University, South Korea, in 2003, and the M.S. and Ph.D. degrees in computer science from Gwangju Institute of Science and Technology, South Korea, in 2005 and 2010, respectively. He is currently a Principal Researcher with the Electronics Telecommunications and Research Institute (ETRI), South Korea. His research interests include diagnosis, anomaly detection, deep learning, and uncertainty.

YU MIN HWANG (Member, IEEE) received the B.S. and Ph.D. degrees from the Department of Wireless Communications Engineering, Kwangwoon University, Seoul, South Korea, in 2012 and 2018, respectively. He was a Postdoctoral Research Fellow with the Department of Electrical and Computer Engineering, Western University, Canada, from 2019 to 2020. He is currently with the Electronics and Telecommunications Research Institute (ETRI), South Korea. His research interests include object recognition, object tracking, deep learning, and anomaly detection.

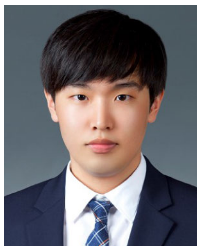

JUNGI LEE received the B.S. degree in EECS from the GIST College, South Korea, in 2014, and the M.S. degree in EECS from GIST, South Korea, in 2017. He is currently a Researcher with the Electronics and Telecommunications Research Institute (ETRI), South Korea. His research interests include embodied AI for robotics, large language models, and machine learning.

NAC-WOO KIM received the B.S. degree in control and instrumentation engineering and the M.S. and Ph.D. degrees in image engineering from Chung-Ang University, South Korea, in 1997, 2002, and 2006, respectively. He is currently a Principal Researcher with the Electronics and Telecommunications Research Institute (ETRI), South Korea. His research interests include data engineering, machine learning, and anomaly detection.

SEOK-KAP KO received the B.S., M.S., and Ph.D. degrees in information telecommunication engineering from Soongsil University, South Korea, in 1997, 2002, and 2009, respectively. Since 2008, he has been a Principal Research Engineer with the Electronics and Telecommunications Research Institute (ETRI), South Korea. His research interest includes machine learning for energy management systems.